Growth and optical properties of Cu_2ZnSnS_4 decorated reduced graphene oxide nanocomposites

Dheivasigamani Thangaraju,[†*] Rajan Karthikeyan,[‡] Natarajan Prakash,[‡] Sridharan Moorthy Babu[§] and Yasuhiro Hayakawa[†,‡,**]

[†]Research Institute of Electronics, Shizuoka University, Hamamatsu 432-8011, Japan

[‡]Graduate School of Science and Technology, Shizuoka University, Hamamatsu 432-8011, Japan

[§]Crystal Growth Centre, Anna University, Chennai-600025, India

Corresponding author
** E-mail: royhaya@ipc.shizuoka.ac.jp (Yasuhiro Hayakawa)
 Tel/Fax: +81 53 478-1310

* E-mail: dthangaraju@gmail.com (Dheivasigamani Thangaraju)
 Tel/Fax: +81 53 478-1338

Growth and optical properties of Cu$_2$ZnSnS$_4$ decorated reduced graphene oxide nanocomposites

Abstract

Cu$_2$ZnSnS$_4$ (CZTS) nanoparticles were synthesized by the precursor injection method using oleylamine as a solvent. Preliminary characterizations indicated that the synthesized nanoparticles belonged to the kesterite structure with a bulged sphere-like morphology. Reduced graphene oxide (rGO) was synthesized by an improved Hummers method and were used for nanoparticle functionalization. CZTS nanocrystals were decorated on rGO by two different methods. One was oleylamine-based nanoparticle functionalization, and the other was *in situ* nanoparticle growth. Transmission electron microscopy analysis of CZTS-functionalized rGO showed that the synthesized nanoparticles were uniformly spread on the surface of rGO sheets. Single phase CZTS nanoparticles were grown on rGO without any impurity phases in the *in situ* growth. Tuned absorption of the pure CZTS was observed by the decoration of CZTS nanoparticles on the surface of rGO in the visible and UV regions.

1. Introduction

Two-dimensional (2D) composite nanostructures have received considerable attention for use in future ultrathin photodetectors.[1–4] Solution-processed photodetecting devices have multiple advantages, such as easy deposition, hand manipulation, and low-cost instrumentation.[5–7] Hybrid 2D materials grown on graphene possess excellent dimensional-dependent properties, like low-cost fabrication and an environmentally friendly nature.[8] In recent scenarios, semiconductor/graphene hybrid composite preparations are in development to enhance the light detection properties of graphene-related materials, even under low-intensity light, which increases the electrical carriers per incident photon.[9] Graphene is a 2D carbon material that offers typical advantages like charge carrier generation by wide energy photon absorption (from ultraviolet to terahertz spectral regions), ultrafast carrier dynamics, electrostatic doping, and low dissipation rate with high mobility in photonics and optoelectronic devices.[10] However, the low photo response, fast carrier dynamics, and poor light absorption of graphene reduce the performance of graphene-based optoelectronic devices.[11,12] These semiconductor nanoparticles in graphene hybrid-related materials have sensitizing centers for efficient absorption of incident light and increased transfer of electrons and holes to the conductor. PbS, CdS, and ZnO materials have been used to sensitize graphene for better light absorption in hybrid photoconductive optoelectronic devices.[13,14] Better light absorption and charge transfer performance of these hybrid systems were previously reported with high quantum efficiency (~25%).[1] Low-intensity light (10–14 W) over a wide light bandwidth were detected by these semiconducting/graphene hybrids.

Recently, reduced graphene oxide (rGO) has received priority in photodetection applications because it provides better ON/OFF ratio, response, and detection because of internal crystal defects.[15] The electronic properties of chemically synthesized GO can be tuned from insulator to semiconducting or semi-metallic by chemical or thermal reduction.[16]

3

Graphene-related materials are synthesized by epitaxial growth, chemical vapor deposition, mechanical exfoliation, and chemical synthesis methods.[17–19] Among the synthesis methods, chemical synthesis of graphene-related materials is low cost and scalable. Few-layered GO sheets have been synthesized by Hummer's method and thermally or chemically reduced to make rGO. The light absorption characteristics of rGO are much better than that of graphene, which helps to improve the performance of photodetection applications.[20]

Earth abundant and quaternary chalcogenide semiconductors are the next generation low-cost and environmentally friendly optoelectronic materials.[21,22] Cu_2ZnSnS_4 (CZTS) is a p-type material with a direct band gap energy of ~ 1–1.6 eV and high absorption coefficient (~10^4 cm^{-1}). CZTS nanoparticles are potential materials for photodetecting applications.[23] Growth of single-phase CZTS is still challenging because of a high tendency to form binary and ternary compounds during the synthesis. An appropriate mixing temperature for the sulfur precursor in the cationic solution and synthesis temperature with appropriate solvent are very important factors for the synthesis of single-phase CZTS. In this article, we report the functionalization of a CZTS NP-decorated rGO hybrid nanocomposite by oleylamine-based nanoparticle functionalization and *in situ* nanoparticle growth methods. The absorption properties of the synthesized CZTS functionalized rGO nanocomposites were characterized by diffuse reflectance measurements.

2. Experimental section

2.1. Materials

Copper (II) acetate monohydrate ($Cu(CH_3COO)_2.H_2O$; 99%), zinc acetate ($Zn(CH_3COO)_2$), tin (II) chloride ($SnCl_2$; 99.9%), sulfur, graphite flakes (99.99%), sulfuric acid (H_2SO_4), phosphoric acid (H_3PO_4), potassium permanganate ($KMnO_4$, 99.3%), hydrogen peroxide (H_2O_2), hydrochloric acid (HCl), and hydrazine monohydrate ($H_2NNH_2.H_2O$) were used as purchased from Wako Pure Chemical Industries Ltd., Japan. Oleylamine (technical

grade, 70%) was purchased from Aldrich. Water for synthesis of rGO was purified by a Milli-Q plus water purification system.

2.1. Synthesis of single-phase CZTS nanoparticles

Pure CZTS NPs were prepared by the precursor injection method. Initially, precursors of $Cu(CH_3COO)_2 \cdot H_2O$ (2 mmol), $Zn(CH_3COO)_2$ (1 mmol), and $SnCl_2$ (1 mmol) were mixed with 5 mL of oleylamine in three-necked flask A (100 mL) equipped with a cooling condenser at room temperature. At the same time, sulfur metal was dissolved in 5 mL of oleylamine in three-neck flask B (100 mL). The temperature of these two reaction mixtures was increased to 140 °C and was thoroughly degassed under vacuum for 30 min to remove moisture and O_2 in oleylamine. The degassed mixture in flask A turned a transparent light blue in color. During this period, the vacuum was released and the chamber was filled with nitrogen gas. Degassed 5 mL of reaction mixture B was loaded to a quartz glass syringe and injected into reaction mixture A. The complete mixture was heated to 270 °C and kept for 90 minutes. The resultant colloids were eventually cooled to 80 °C, and a sufficient amount of ethanol was added to dilute the mother solution. The colloids were isolated by centrifugation and thoroughly washed with ethanol for two cycles.

2.2. Synthesis of reduced graphene oxide nanosheets (rGO)

The rGO was synthesized from 150 μm graphite flakes by an improved version of Hummer's method. A mixture of concentrated H_2SO_4/H_3PO_4 (120/15 mL) was added to a mixture of graphite flakes (1.0 g) under stirring for 30 min. $KMnO_4$ (6 g) was added to the above mixture at 0 °C. It was heated to 40–45 °C for about 15 h, cooled down to room temperature, and poured into approximately 120 mL of distilled water. With the addition of distilled water, oxidation was initiated. To terminate the reaction, H_2O_2 (3 mL) was added to the above mixture. The mixture was filtered, and the filtrate was washed with a succession of 100 mL of water and 100 mL of 30% HCl several times. The resultant product was vacuum-

dried for 12 h at room temperature to obtain the final product. To prepare rGO, synthesized GO (200 mg) was dispersed in de-ionized water, to which a certain amount of hydrazine hydrate was added, and the mixture was refluxed for 12 h. The product was washed several times with de-ionized water and vacuum dried.

2.3. Synthesis of CZTS NP- functionalized rGO nanocomposite

2.3.1 Oleylamine-based CZTS- functionalized rGO (O-rGO/CZTS)

Synthesized CZTS (100 μL) was dispersed in 10 mL of cyclohexane. Then, 10 mg of rGO and 200 μL of oleylamine were added to the above solution and the mixture was ultra-sonicated for 2 h. The final solution was centrifuged with an equal volume of ethanol. The obtained product was washed two times with ethanol and redispersed in cyclohexane for further studies.

2.3.2. *In situ* growth of CZTS-decorated rGO (I-rGO/CZTS)

As-synthesized rGO (10 mg) was dispersed in 2 mL of cyclohexane and 5 mL of oleylamine and was ultrasonicated for 30 min. The rGO dispersed oleylamine solution was degassed for 1 h to remove cyclohexane in a neck flask. The metal precursors $Cu(CH_3COO)_2 \cdot H_2O$ (2 mmol), $Zn(CH_3COO)_2$ (1 mmol), and $SnCl_2$ (1 mmol) were mixed with the above solution and degassed for another 30 min at 140 °C. Sulfur (4 mmol) was degassed at 140 °C in a separate container and was injected into the rGO metal precursor solution. The temperature of the mixture was further raised to 270 °C and kept for 1 h. The final solution was cooled down to 80 °C and washed with ethanol two times.

2.4. Instrumentation

The crystal structure of synthesized nanoparticles was determined by powder X-ray diffraction (XRD) with a scan rate of 0.04° s^{-1} in the 2θ range from 10° to 80° using a Rigaku (Japan) X-ray diffractometer (RINT-2200, CuKα radiation, λ =1.54178 Å). The morphology and size of the derived particles were examined by transmission electron microscopy (TEM)

and high-resolution TEM (HRTEM) using a JEOL TEM 2100F microscope at an accelerating

voltage of 200 kV. Chemical structure analysis was conducted by X-ray photoelectron

spectroscopy (XPS) using a Shimadzu ESCA 3100 spectrophotometer. Fourier transform

infrared spectroscopy (FTIR) spectra were obtained using a JEOL JIR-WINSPEC 50

spectrometer. Raman spectra of the derived samples were measured by a JASCO NRS-7100

laser Raman spectrometer under 532 nm excitation. The diffused reflectance spectrum was

recorded by a JASCO V-670 spectrophotometer with an ISN-723 integrating sphere

accessory.

3. Results and discussion

3.1. Characterization of single-phase CZTS NPs

Powder XRD was performed to confirm the crystalline phase of the synthesized CZTS

NPs, as shown in Fig. 1(a) and (b). The diffraction peaks of as-synthesized CZTS

nanoparticles were well matched with the kesterite structure of CZTS. For comparison,

standard PDF No: 00-026-0575 was indexed in the same figure. Un-reacted sulfur (S) and

copper sulfate ($Cu_{2-x}S$) peaks were not observed in the XRD patterns.[24]

The Raman spectrum of as-synthesized CZTS NPs is shown in Fig. 1(c). All the observed

peaks of CZTS NPs were well matched with the vibrational modes of the kesterite CZTS

phase. The intense peak at 333 cm^{-1} was assigned to the A^1 mode, which is the strongest

mode observed from kesterite CZTS. A peak near 283 cm^{-1} corresponded to the A^2 mode,

and the peaks located at approximately 268, 361, and 371 cm^{-1} were weaker vibrational

modes of CZTS, identified as the B/E, B, and B modes, respectively.[25,26] The less intense

peak observed near 475 cm^{-1} was related to $Cu_{2-x}S$. This confirms that there was a slight trace

of $Cu_{2-x}S$ in the final product, but this was not observed in the XRD patterns. No significant

peaks related to Cu_2SnS_3 at 318 cm^{-1} were observed in the spectrum, implying the kesterite

phase was present.

Fig. 2(a), (b) and (c) show typical TEM, HRTEM and particle size distribution of as-

synthesized CZTS NPs. The TEM image of CZTS (Fig. 2(a)) revealed that the morphology of

the derived nanoparticles was like a bulging spheres. Fig. 2(b) presents an HRTEM image of

CZTS particles, with an interplanar distance of 3.125 Å, suggesting that this belongs to the

(112) lattice distance of CZTS. Particles size distribution of the CZTS nanoparticles was

calculated for 100 nanoparticles and their sizes were ranged between 10 to 40 nm.

XPS analysis was performed to study the valence states of elements present in the

synthesized CZTS samples. Fig. 3(a)–(d) show the XPS peaks of Cu 2p, Zn 2p, Sn 3d, and S

2p. Two peaks were observed in the Cu 2p region at 932.7 eV ($2p_{3/2}$) and 952.6 eV ($2p_{1/2}$),

which can be attributed to the valance state of copper in CZTS of +1. Zn 2p split into two

peaks at 1022.2 and 1044.1 eV, which corresponded to the binding energies of Zn $2p_{3/2}$ and

Zn $2p_{1/2}$. This binding energy value indicated a +2 valence for Zn. The valence state of Sn

was identified as +4, with two Sn $3d_{5/2}$ and Sn $3d_{3/2}$ peaks at 486.1 and 492.7 eV,

respectively. Two overlapping peaks of S $2p_{3/2}$ (161.8 eV) and $2p_{1/2}$ (162.5 eV) revealed the -

2 valence state in CZTS NPs.[27,28]

3.2. Characterization of oleylamine/reduced graphene oxide (OA/rGO)

The properties of chemically synthesized rGO capped with oleylamine were examined

with XRD and TEM analysis, as shown in Fig. 4(a)–(b). Fig.4(a) shows the XRD pattern of

OA/rGO. A broad peak near 25.5° and a low intense peak at 43.1° can be attributed to the

(002) and (100) planes of chemically rGO. The calculated interlayer distance was 3.493 Å,

which matched well with that of previously reported rGO.[29] TEM images of OA/rGO clearly

show the sheet-like morphology of the material, as shown in Fig. 4(b). Fig. 5 shows the XPS

C1s spectra of OA/rGO, where the blue line shows the experimental data and the red dotted line shows the fit sum. The XPS spectrum was composed of six Gaussian peaks related to carbon bonds. C-C bonds appeared at 284.52 and 284.95 eV, corresponding to sp^2 and sp^3 hybridized carbon peaks, respectively. These values agreed well with previously reported rGO.[30] C-N bonds appeared near 286.05 eV, and oxygen-related C-O, C=O, and C(O)OH bonds were located at 286.95, 288.08, and 290 eV, respectively.[31] The low intensity of oxygenated carbon peaks confirmed the formation of rGO. The appearance of a C-N peak in the C 1s core spectrum indicated the encapsulation of oleylamine over the surface of the rGO sheet. Oleylamine is one of the best intercalating agents used to exfoliate graphene-related materials. The effectiveness of the oleylamine cap over the surface of the rGO was further evaluated with FTIR spectra as shown in Fig. 6. Absorption bands located at 3317 cm^{-1} can be assigned to the stretching vibrations of C-OH, COOH, and H_2O. The highly intense absorption bands near 2914 and 2850 cm^{-1} correspond to the vibrations of C-H because of the CH_2 and CH_3 presence in oleylamine. Bending vibrations of C-H were observed at 1472 cm^{-1}. Strong absorption bands related to C-N and N-H stretching modes were observed at 1326 and 1557 cm^{-1}, respectively.[32] This indicated that rGO sheets were capped with oleylamine. The bands related to -OH, C-O and C-O-C of oleylamine capped rGO showed low intense when compared to uncapped rGO. The low intense stretching vibration bands indicated that the presence of oxygenated carbon was very low.[33]

3.3. Characterization of CZTS NP-decorated rGO nanocomposite

CZTS-decorated rGO was synthesized by two methods. One was oleylamine-assisted sticking of CZTS NPs under ultrasonication (O-rGO/CZTS), and the other was *in situ* growth of CZTS NPs on the surface of rGO sheets (I-rGO/CZTS). Fig. 7 shows the comparative XRD patterns of O-rGO/CZTS, I-rGO/CZTS, and standard CZTS. The diffraction peaks of O-rGO/CZTS indicated overlapping of the CZTS reflection over the rGO broad peaks, which

confirmed the presence of rGO and CZTS in the nanocomposite. XRD patterns of the I-rGO/CZTS nanocomposite were indexed to the kesterite phase of CZTS, which was well matched with the standard patterns. There were no other crystalline impurities in the synthesized product. Less intense rGO-related peaks overlapping with CZTS were seen in the diffraction pattern, indicating that rGO was exfoliated and reduced at high temperature.

The distribution nature and assembling behavior of the O-rGO/CZTS and I-rGO/CZTS nanocomposites were examined by TEM and HRTEM analysis; the micrographs are displayed in Fig. 8 and Fig. 9. TEM and HRTEM images of O-rGO/CZTS reveal that the synthesized particles are evenly conjugated on the surface of the rGO sheets. Fig. 8(a), (b) and (c) show that the particles were evenly distributed on the surface of the rGO sheet. TEM images of I-rGO/CZTS (Fig. 9(a)–(d)) confirm the formation of CZTS particles on the surface of the rGO sheets, indicating that *in situ* growth leads to a highly dense distribution of particles on the surface of the rGO sheets. Fig. 9(a) and (b) confirm that the particle growth took place on the surface of the rGO sheet. The high-magnification view of I-rGO/CZTS in Fig. 9(c) confirms the growth of particles at the edges of rGO sheets. The HRTEM image of I-rGO/CZTS (Fig. 9(d)) indicates a lattice distance of 3.12 Å, corresponding to the (112) plane of the CZTS kesterite phase. Compared with normal growth of CZTS, rGO-assisted growth led to uniform sphere-like particles, which were uniformly distributed over the surface of the rGO.

Comparative Raman spectra of as-synthesized rGO, O-rGO/CZTS, and I-rGO/CZTS are presented in Fig. 10. Two remarkable peaks at 1347 and 1594 cm^{-1} were observed for O-rGO/CZTS, and peaks at 1372 and 1586 cm^{-1} appeared for I-rGO/CZTS, which corresponded to the D and G bands, respectively. The G band shows the E_{2g} vibration mode of sp^2 carbon, and the D band is associated with the defects and disordered structure of sp^2 carbon. The I_D/I_G

ratio of the synthesized O-rGO/CZTS sample was 0.931, and it decreased to 0.644 for the I-rGO/CZTS sample. An intensity decrease in the D band was observed for O-rGO/CZTS and I-rGO/CZTS when compared with as-synthesized rGO. This indicated that the orderedness increased in *in situ* growth of CZTS on rGO because of the healing effect of oleylamine at high temperatures.[31,34] CZTS-related peaks were observed between 300 and 370 cm^{-1} for I-rGO/CZTS samples; however, small humps were observed for O-rGO/CZTS because of the low concentration of CZTS NPs present on the surface of rGO.

A possible mechanism for the *in situ* growth of CZTS on the surface of the rGO in oleylamine solvent is given in the schematic diagram shown in Fig. 11. In oleylamine based CZTS functionalization, oleylamine with rGO was added to achieve a uniform dispersion in organic solvent. Further mixing of oleylamine capped CZTS made a non-covalent hydrophobic attachment on the surface of the rGO.[35] In *in situ* growth, mixing of rGO with the oleylamine/cyclohexane solvent was intercalated under ultra-sonication and dispersed well. The Cu, Zn, and Sn metal precursors were added to the rGO/oleylamine solution and heated to 140 °C under degassing. A metal-oleylamine complex was formed during the heating process.[36,37] The metal-oleylamine complex was dispersed on the rGO sheets in oleylamine solvent. Mixing of sulfur and oleylamine at low temperatures produced alkylammonium polysulfides. When it was heated to high temperatures, H_2S was produced, along with thioamides. The metal ions readily reacted with H_2S and formed metal sulfide nanocrystals.[38] These H_2S molecules were adsorbed on the defective sites of the rGO.[39] Sulfur atoms bonded to the carbon atoms at defect sites on the rGO surface and released hydrogen molecules.[40] These bonded sulfur ions formed the crystalline sites for the growth of CZTS on the surface of rGO.

Fig. 12(a) and (b) represent the diffused reflectance and absorption spectra of as-synthesized CZTS, O-rGO/CZTS, and I-rGO/CZTS. The as-prepared CZTS sample showed a higher absorption in the visible region between 340 and 600 nm, and the sharp decrease at approximately 650 nm shows the absorption edge. Lower absorption was observed near 1200 nm for the CZTS sample.[41] The absorption edge of the I-rGO/CZTS sample shifted toward the lower wavelength region when compared with as-synthesized CZTS. The presence of rGO altered the reflectance pattern of CZTS in the red region. The reflectance pattern of O-rGO/CZTS showed high reflectivity (86.7%) in the IR region, and reflectivity gradually decreased at lower wavelengths. Decoration of CZTS NPs on the surface of rGO increased absorption in the visible and UV regions. The reason for the absorption difference is represented in the schematic diagram of CZTS, I-rGO/CZTS and O-rGO/CZTS absorption (Fig. 13). CZTS nanoparticles have high absorption in the visible region (Fig. 13 (a)). A 2D nanocomposite-like structure was formed, when CZTS adsorbed on the rGO. The CZTS particles were densely populated on the surface of the rGO sheets in *in situ* growth method (Fig. 13 (b)). On the other hand, oleylamine-based nanoparticle functionalization leads the spatial location of CZTS on the surface of the rGO sheets (Fig. 13 (c)). This 2D composite structures lead tunability in absorption properties of CZTS.

4. Conclusion

CZTS NP decorated rGO nanocomposite were successfully synthesized by a simple oleylamine-based functionalization method and *in situ* particle growth method. The obtained products from the precursor injection method were single phase kesterite CZTS NPs with diameters of 10–30 nm. An improved Hummers method synthesized rGO was sheet like structure and were easily dispersed in cyclohexane/oleylamine mixed solvent. The synthesized particles were homogeneously spread on the surface of the rGO by oleylamine-

based functionalization method. The *in situ* particle growth method enabled the uniform spherical-shaped single phase CZTS nanoparticles on the surface of rGO and was confirmed by XRD, TEM and Raman analysis. The absorption nature of CZTS in the presence of rGO changed in the visible and near IR regions, as identified by diffused reflectance measurements.

Acknowledgments

References

1   G. Konstantatos, M. Badioli, L. Gaudreau, J. Osmond, M. Bernechea, F. P. G. Arquer, F. Gatti, F. H. L. Koppens, *Nat. Nanotechnol.,* 2012, **7**, 363–368.

2   S. R. Tamalampudi, Y. Y. Lu, U. R. Kumar, R. Sankar, C. D. Liao, B. K. Moorthy, C. H. Cheng, F. C. Chou, Y. T. Chen, *Nano Lett.,* 2014, **14**, 2800–2806.

3   X. Li, M.W. Lin, A. Puretzky, J. C. Idrobo, C. Ma, M. Chi, M. Yoon, C. M. Rouleau, I. I. Kravchenko, D. B. Geohegan, K. Xiao, *Sci. Rep.,* 2014, **4**, 5497 (1-9).

4   W. Zhang, M. Chiu, C. H. Chen, W. Chen, L. Li, A. T. S. Wee, *ACS Nano,* 2014, **8**, 8653–8661.

5   X. Wang, W. Tian, M. Liao, Y. Bando, D. Golberg, *Chem. Soc. Rev.,* 2014, **43**, 1400–1422.

6   G. Sarasqueta, K. R. Choudhury, F. So, *Chem. Mater.,* 2010, **22**, 3496–3501.

7   Y. Yuan, Q. Dong, B. Yang, F. Guo, Q. Zhang, M. Han, J. Huang, *Sci. Rep.,* 2013, **3**, 2707 (1-7).

8   J. Li, L. Niu, Z. Zheng, F. Yan, *Adv. Mater.,* 2014, **26**, 1–35.

9   Y. Lin, K. Zhang, W. Chen, Y. Liu, Z. Geng, J. Zeng, N. Pan, L. Yan, X. Wang, J. G. Hou, *ACS Nano,* 2010, **4**, 3033–3038.

10   F. H. L. Koppens, T. Mueller, P. Avouris, A. C. Ferrari, M. S. Vitiello, M. Polini, *Nat. Nanotechnol.,* 2014, **9**, 780–793.

11   W. Li, Y. He, L. Wang, Z. Q. Zhang, R. W. Lortz, P. Sheng, N. Wang, *Phys. Rev. B - Condens. Matter Mater. Phys.,* 2011, **84**, 1–8.

12   M. Zhu,; X. Li, Y. Guo, X. Li, P. Sun, X. Zang, K. Wang, M. Zhong, D. Wu, H. Zhu, *Nanoscale,* 2014, **6**, 4909–4914.

13   Z. Sun, Z. Liu, J. Li, G. A. Tai, S. P. Lau, F. Yan, *Adv. Mater.,* 2012, *24*, 5878–5883.

14   S. M. Jilani, P. Banerji, *ACS Appl. Mater. Interfaces,* 2014, **6**, 16941−16948.

15   Q. P. Luo, X. Y. Yu, B. X. Lei, H. Y. Chen, D. B. Kuang, C. Y. Su, *J. Phys. Chem. C,* **2012**, *116*, 8111–8117.

16   K. P. Loh, Q. Bao, G. Eda, M. Chhowalla, *Nat. Chem.,* **2010**, *2*, 1015–1024.

17   K. V. Emtsev, A. Bostwick, K. Horn, J. Jobst, G. L. Kellogg, L. Ley, J. L. McChesney, T. Ohta, S. A. Reshanov, J. Röhrl, E. Rotenberg, A. K. Schmid, D. Waldmann, H. B. Weber, T. Seyller, *Nat. Mater.,* **2009**, *8*, 203–207.

18   R. Muñoz, C. Gómez-Aleixandre, *Chem. Vap. Depos.,* **2013**, *19*, 297–322.

19   K. S. Novoselov, A. K. Geim, S. V. Morozov, D. Jiang, Y. Zhang, S. V. Dubonos, I. V. Grigorieva, A. A. Firsov, *Science,* 2004, *306*, 666–669.

20   G. Eda, M. Chhowalla, *Adv. Mater.,* 2010, *22*, 2392–2415.

21   C. Wang, S. Chen, J. H. Yang, L. Lang, H. J. Xiang, X. G. Gong, A. Walsh, S. H. Wei, *Chem. Mater.,* 2014, *26*, 3411–3417.

22   C. Zou, L. Zhang, D. Lin, Y. Yang, Q. Li, X. Xu, X. Chena, S. Huang, *CrystEngComm.,* 2011, **13**, 3310-3313.

23   J. J. Wang, J. S. Hu, Y. G. Guo, L. J. Wan, *NPG Asia Mater.,* 2012, *4*, e2 (1-6).

24   S. C. Riha, B. A. Parkinson, A. L. Prieto, *J. Am. Chem. Soc.,* 2009, *131*, 12054–12055.

25   J. He, L. Sun, Y. Chen, J. Jiang, J. Chu, *RSC Adv.,* 2014, **4**, 43080–43086.

26   A. Khare, B. Himmetoglu, M. Cococcioni, E. S. Aydil, *J. Appl. Phys.,* 2012, **111**, 123704 (1-8).

27   S. Ji, T. Shi, X. Qiu, J. Zhang, G. Xu, C. Chen, Z. Jiang, C. A. Ye, *Sci. Rep.,* 2013, **3**, 2733 (1-7).

28   J. Park, M. Song, W. M. Jung, W. Y. Lee, H. Kim, Y. Kim, C. Hwang, I. W. Shim, *Dalton Trans.,* 2013, **42**, 10545-10550

29   P. Cui, J. Lee, E. Hwang, H. Lee, *Chem. Commun.,* 2011, **47**, 12370–12372.

30   R. Su, S. F. Lin, D. Q. Chen, G. H. Chen, *J. Phys. Chem., C* 2014, **118**, 12520–12525.

31   S. Some, Y. Kim, Y. Yoon, H. Yoo, S. Lee, Y. Park, H. Lee, *Sci. Rep.,* 2013, **3**, 1929 (1-5).

32   H. Wu, W. Chen, *Nanoscale,* 2011, **3**, 5096-5102.

33   S. Yang, J. Dong, Z. Yao, C. Shen, X. Shi, Y. Tian, S. Lin, X. Zhang, *Sci. Rep.,* 2014, **4**, 4501 (1-6).

34   O. K. Park, Y. M. Choi, J. Y. Hwang, C. M. Yang, T. W. Kim, N. H. You, H. Y. Koo, J. H. Lee, B. C. Ku, M. Goh, *Nanotechnology,* 2013, **24**, 185604 (1-7).

35   E. Peng, E. S. G. Choo, P. Chandrasekharan, C. T. Yang, J. Ding, K. H. Chuang, J. M. Xue, *Small,* 2012, **8**, 3620–3630.

36   S. Mourdikoudis, L. M. Liz-marza, *Chem. Mater.,* 2013, **25**, 1465–1476.

37   T. Sreethawong, K. W. Shah, S. Zhang, E. Ye, S. H. Lim, U. Maheswaran, W. Y. Mao, M. Han, *J. Mater. Chem. A,* 2014, **2**, 3417–3423.

38   J. W. Thomson, K. Nagashima, P. M. Macdonald, G. A. Ozin, *J. Am. Chem. Soc.,* 2011, **133**, 5036–5041.

39   D. Borisova, V. Antonov, A. Proykova, *Int. J. Quantum Chem.*, 2013, **113**, 786–791.

40   C. Zhang, W. Lv, W. Zhang, X. Zheng, M. B. Wu, W. Wei, Y. Tao, Z. Li, Q. H. Yang, *Adv. Energy Mater.,* 2014, **4**, 1–5.

41   X. Lu, Z. Zhuang, Q. Peng, Y. Li, *Chem. Commun.,* 2011, **47**, 3141–3143.
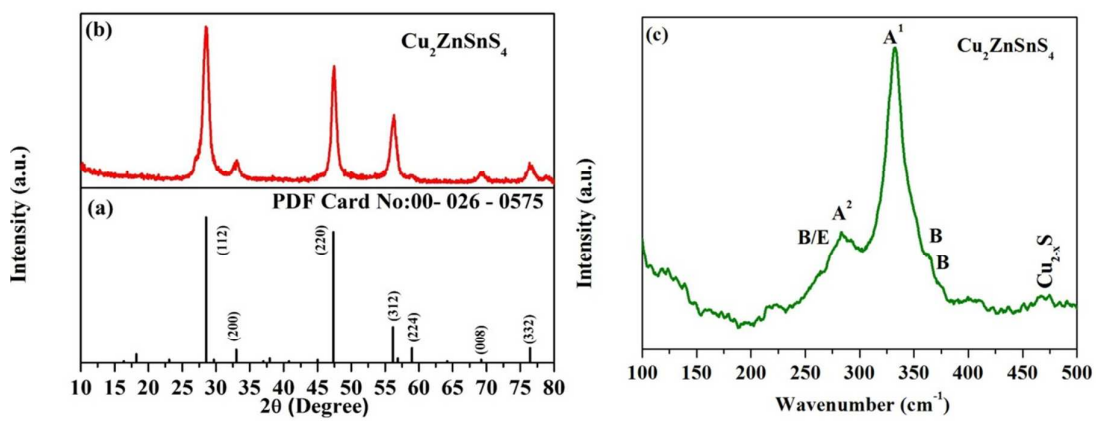
Fig. 1. Powder XRD patterns for standard CZTS, as-synthesized CZTS (b) and Raman spectrum of CZTS (c)
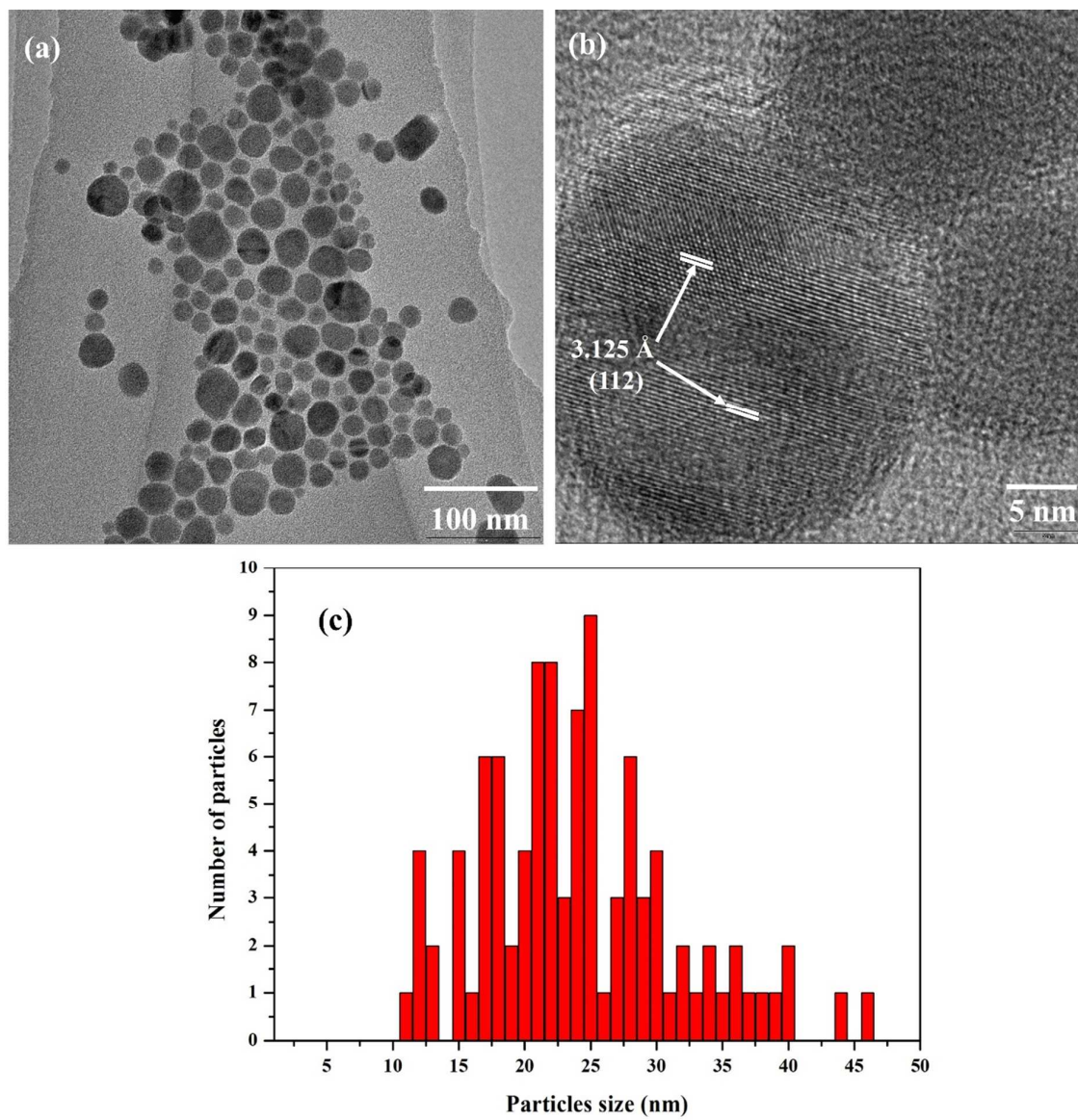
Fig. 2. TEM (a), HRTEM (b) and particle size distribution (c) of synthesized CZTS NPs
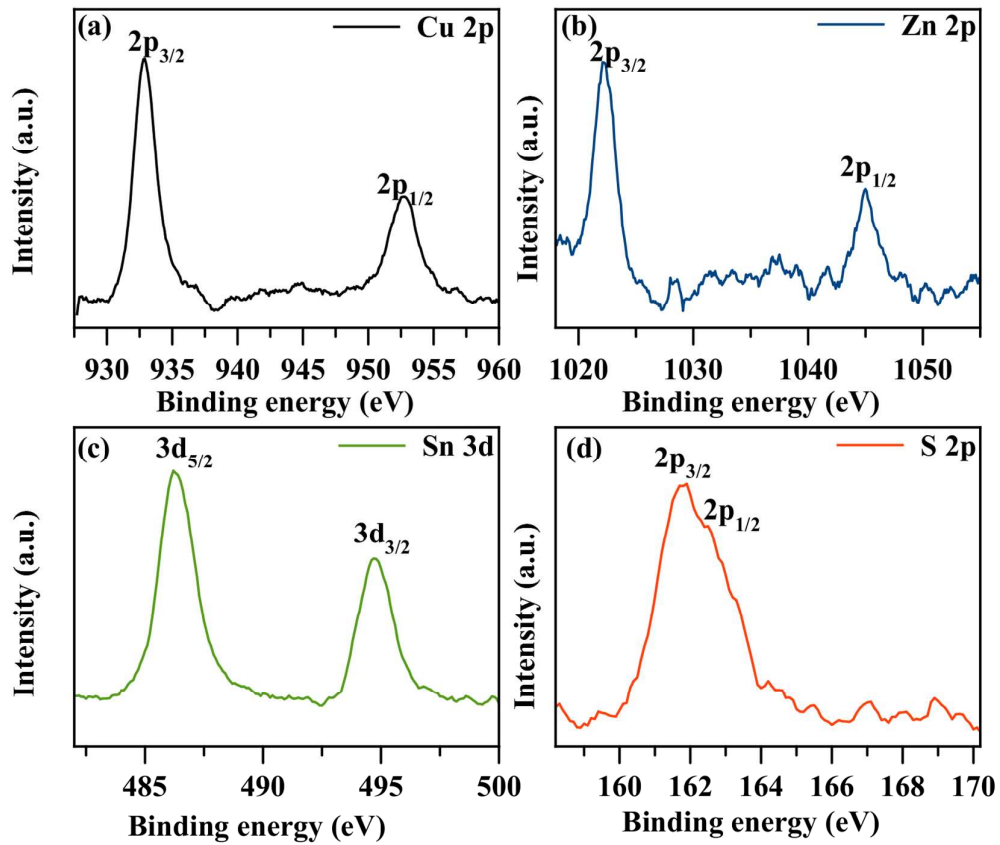
Fig. 3. XPS spectra Cu 2p (a), Zn 2p (b), Sn 3d (c) and S 2p (d) of synthesized CZTS NPs
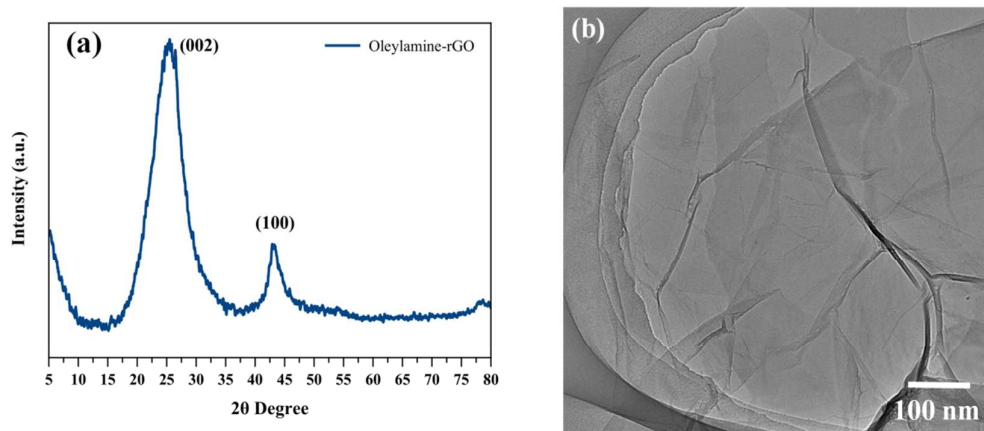
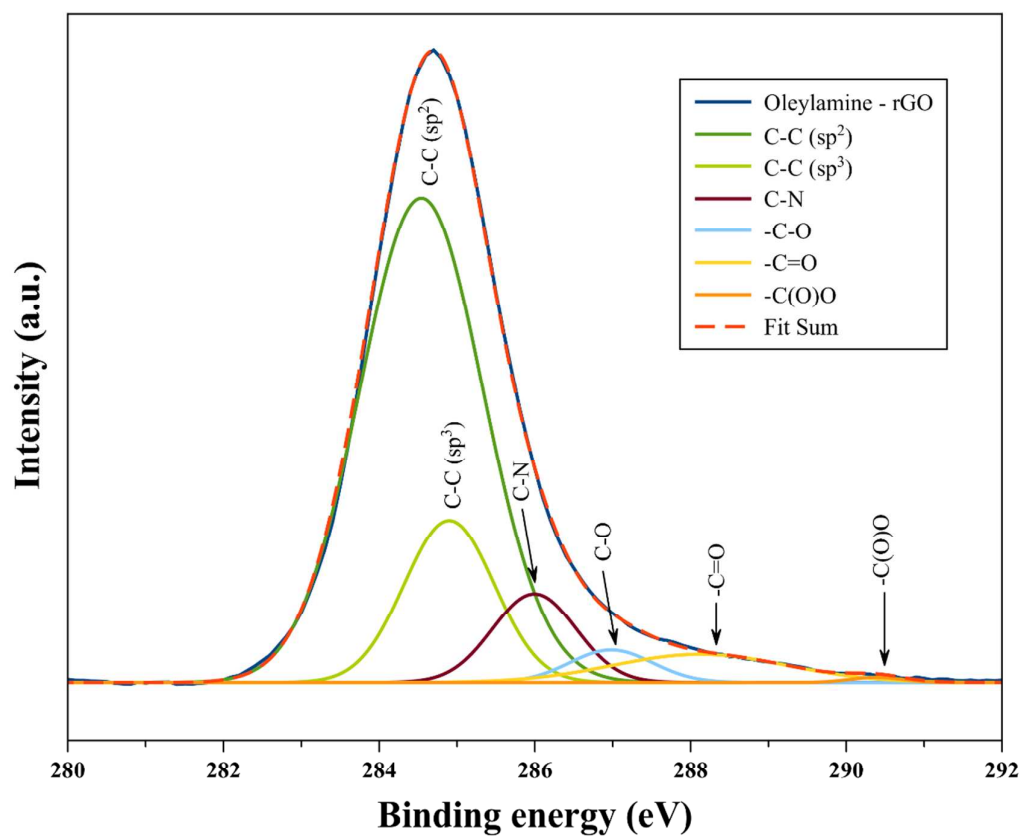Fig. 4. XRD pattern (a) and TEM image (b) of oleylamine capped rGO.

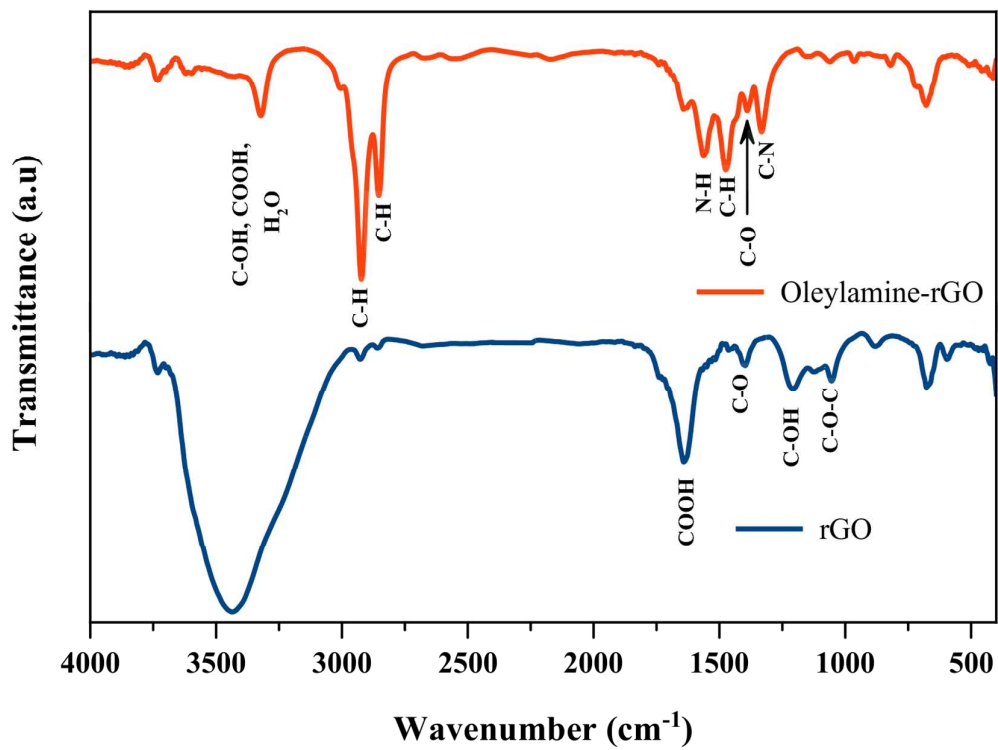Fig. 5. XPS C 1s spectra of oleylamine capped rGO.

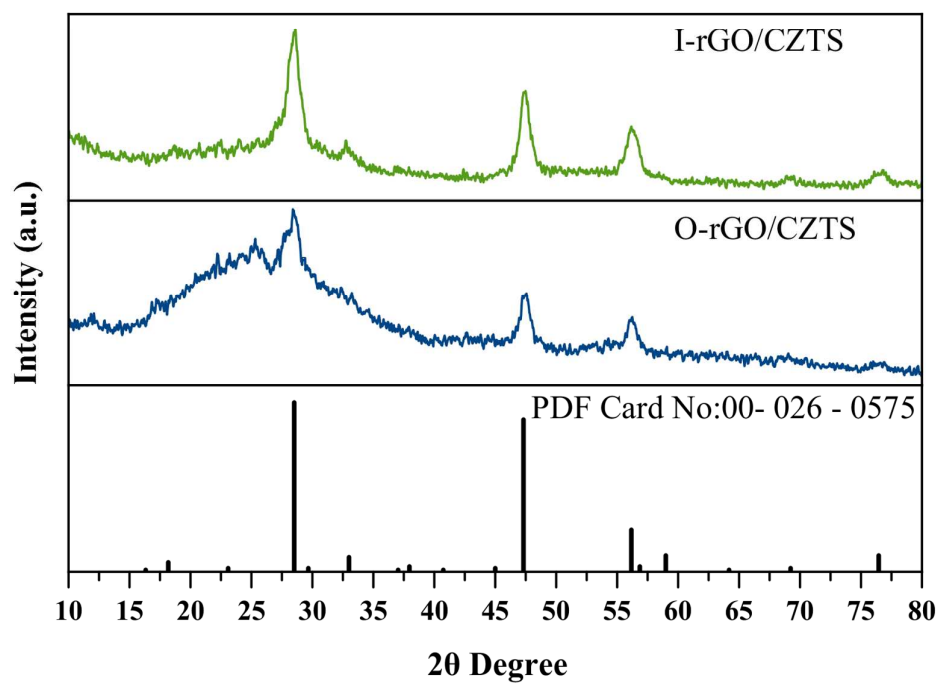Fig. 6. Comparative FTIR spectrum of rGO and oleylamine capped rGO.

Fig. 7. Comparative powder XRD patterns for oleylamine-based O-rGO/CZTS and *in situ* I-rGO/CZTS synthesized nanocomposites
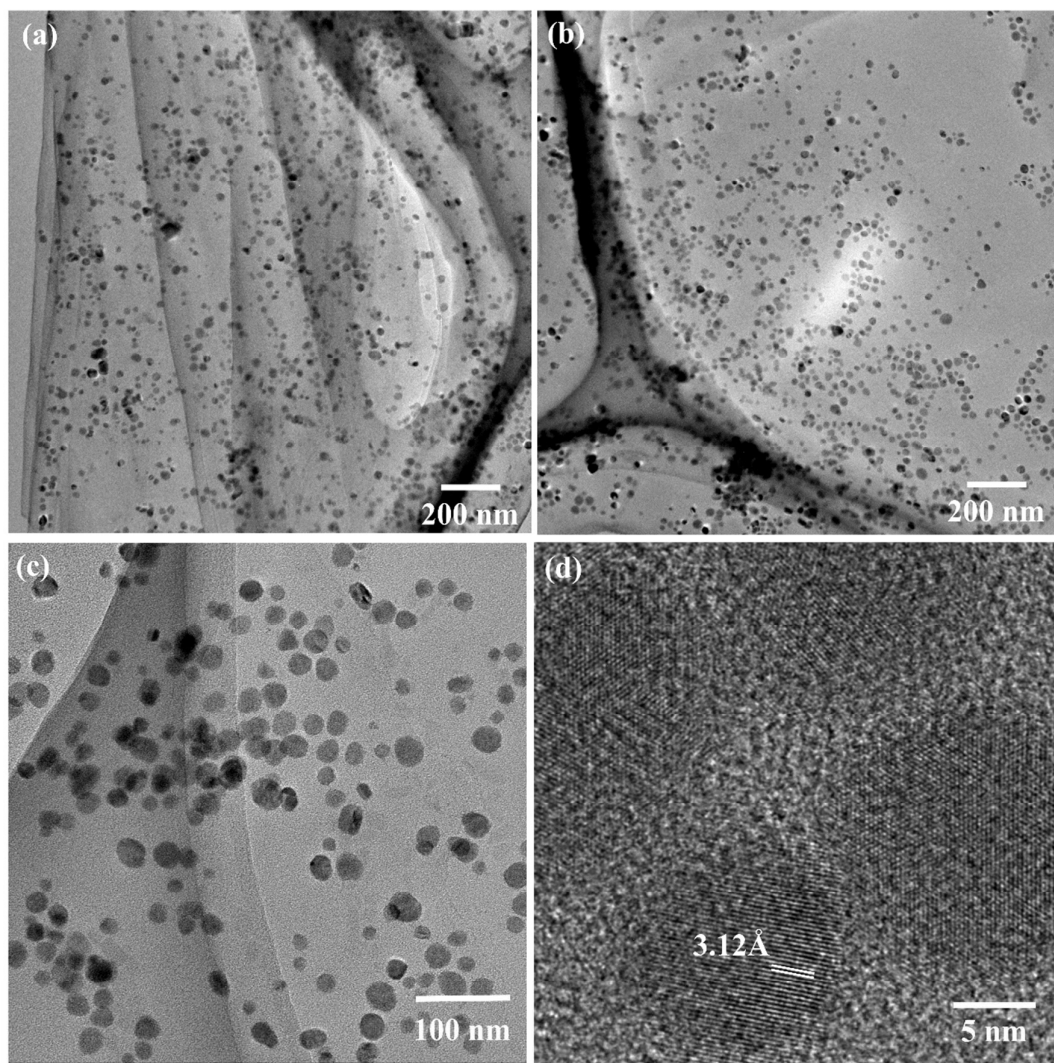
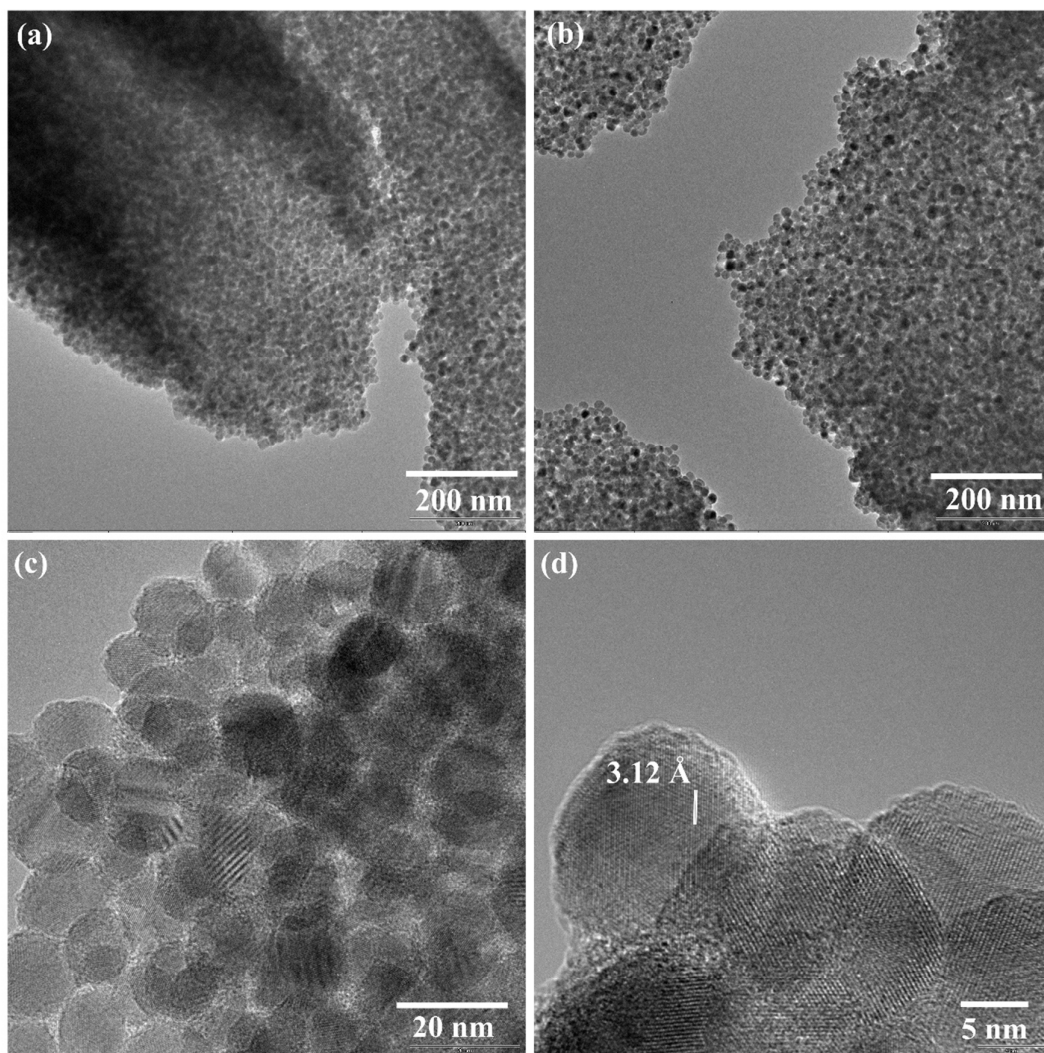Fig. 8. TEM and HRTEM images obtained from O-rGO/CZTS (a, b, c and d) nanocomposites

Fig. 9. TEM and HRTEM images obtained from I-rGO/CZTS (a, b, c and d) nanocomposites
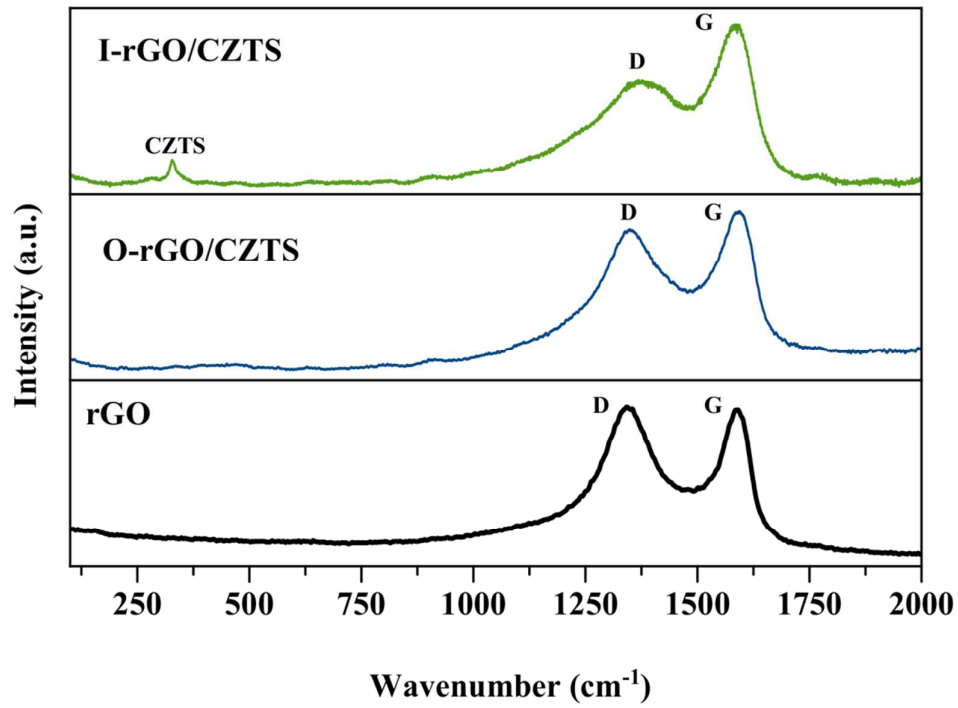
Fig. 10. Comparative Raman spectra for as-synthesized rGO, O-rGO/CZTS, and I-rGO/CZTS nanocomposites
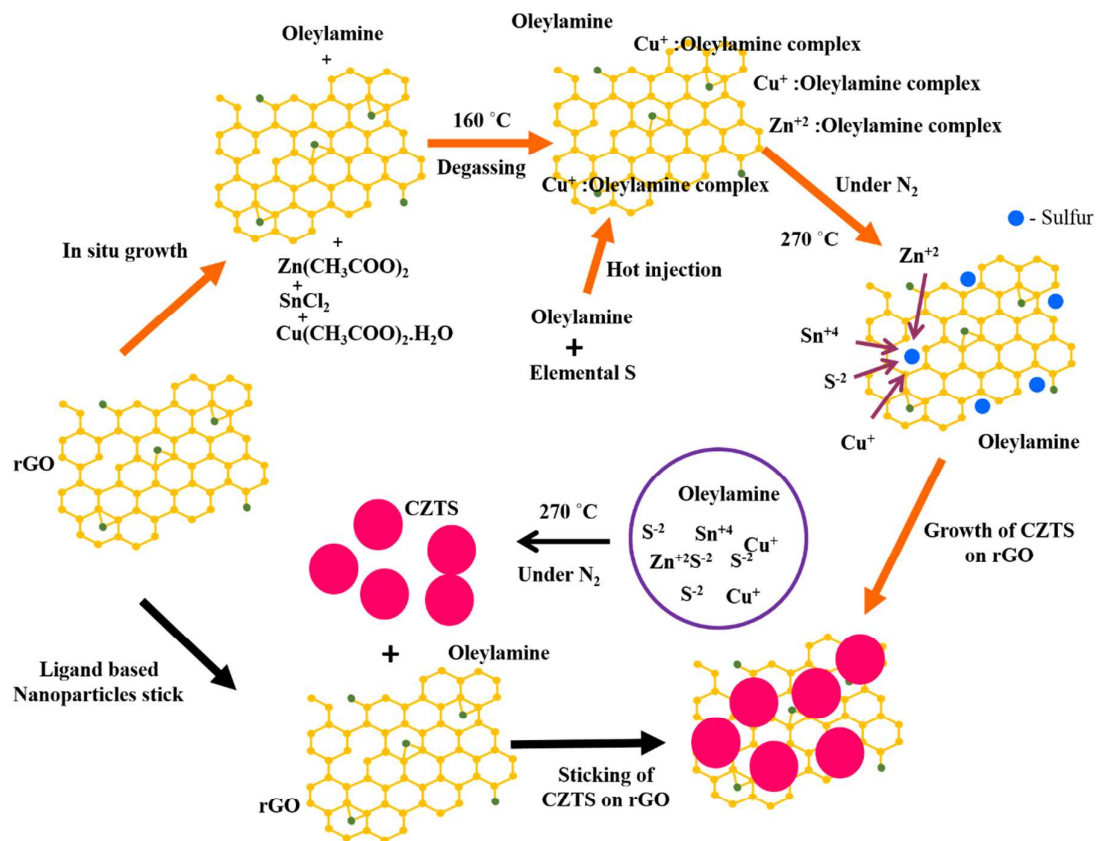
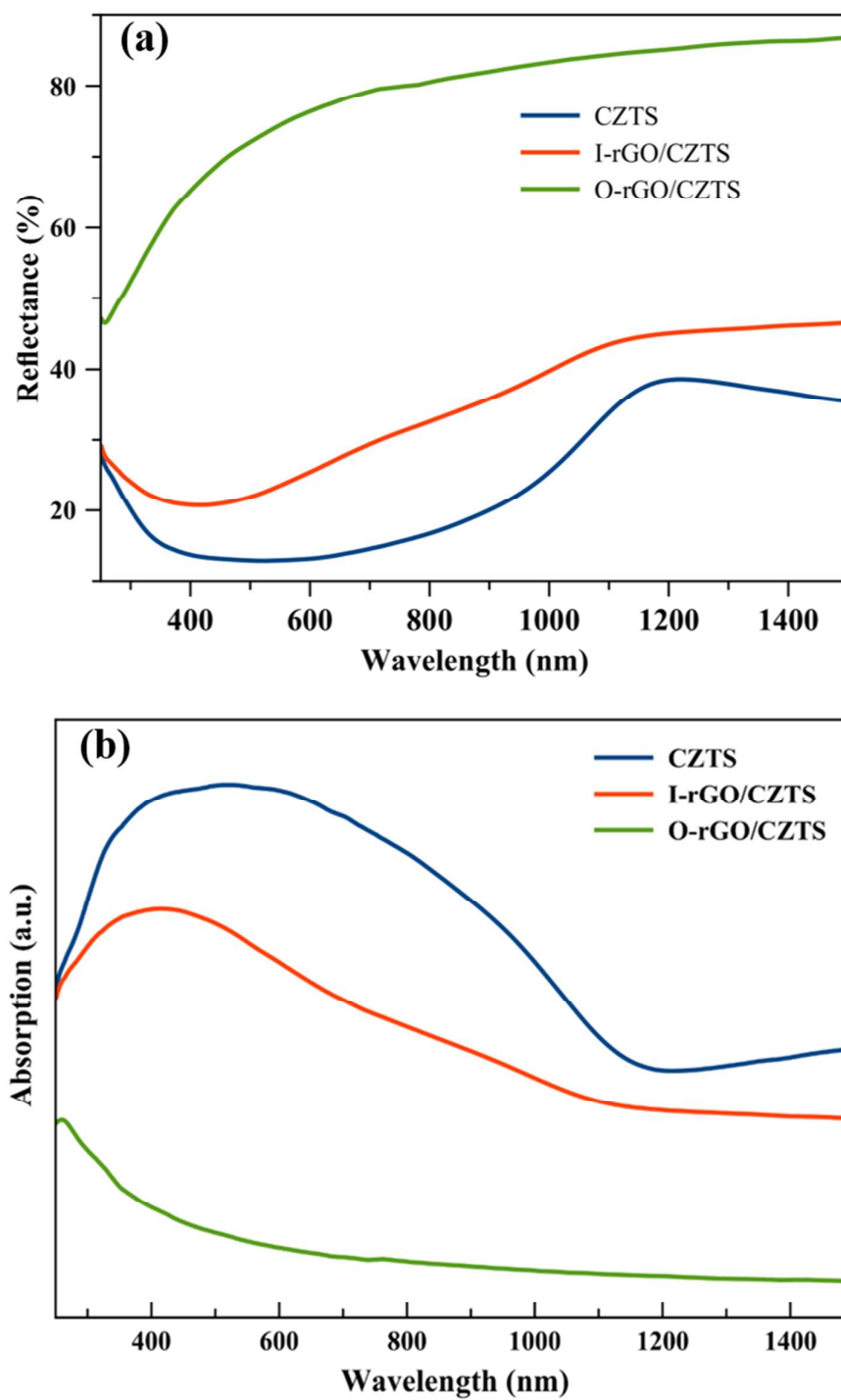Fig. 11. Schematic representation of the growth mechanism of CZTS-decorated rGO

Fig. 12. Comparative diffused reflectance (a) and absorption (b) spectra for as-synthesized CZTS, O-rGO/CZTS, and I-rGO/CZTS

(a)

CZTS

~13 % reflectance in visible region

(b)

I-rGO/CZTS

~21 % reflectance in visible region

(c)

O-rGO/CZTS
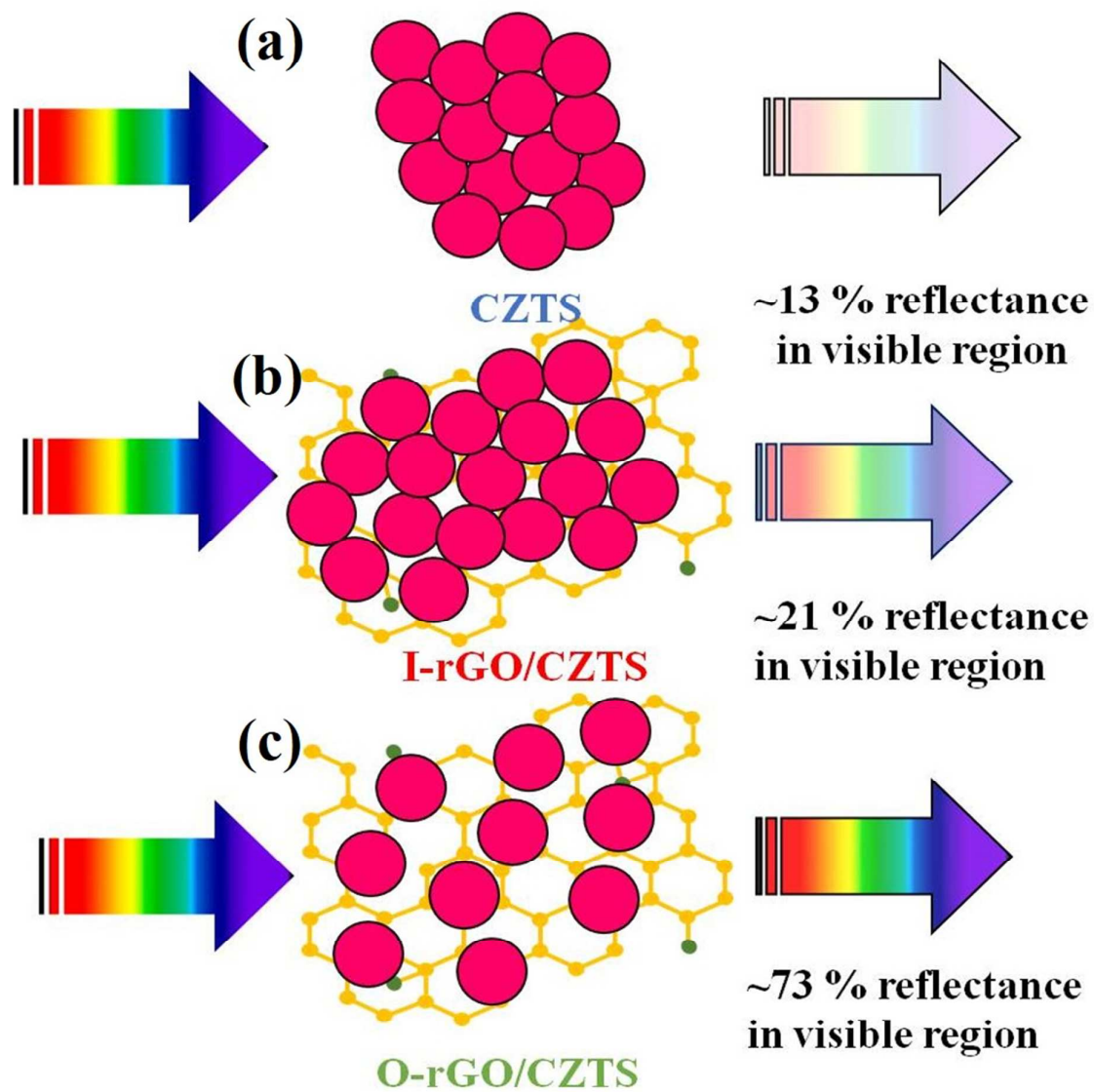
~73 % reflectance in visible region

Fig. 13. Schematic representation of CZTS (a), I-rGO/CZTS (b) and O-rGO/CZTS (c) absorption